Research Article

Nano Research
2022, 15(7): 6054–6061

ISSN 1998-0124 CN 11-5974/O4
https://doi.org/10.1007/s12274-022-4304-8

Carbon-supported high-entropy Co-Zn-Cd-Cu-Mn sulfide nanoarrays promise high-performance overall water splitting

Yuanting Lei[1], Lili Zhang[1], Wenjing Xu[2], Chengli Xiong[1], Wenxing Chen[2], Xu Xiang[3], Bing Zhang[1], and Huishan Shang[1] (✉)

[1] *School of Chemical Engineering, Zhengzhou University, Zhengzhou 450001, China*
[2] *Energy & Catalysis Center, School of Materials Science and Engineering, Beijing Institute of Technology, Beijing 100081, China*
[3] *State Key Laboratory of Chemical Resource Engineering, Beijing University of Chemical Technology, Beijing 100029, China*

Received: 27 January 2022 / **Revised:** 4 March 2022 / **Accepted:** 7 March 2022

ABSTRACT

Transition metal sulfides with homogeneous multi-metallic elements promise high catalytic performance for water electrolysis owing to the unique structure and highly tailorable electrochemical property. Most existing synthetic routes require high temperature to ensure the uniform mixing of various elements, making the synthesis highly challenging. Here, for the first-time novel carbon fiber supported high-entropy Co-Zn-Cd-Cu-Mn sulfide (CoZnCdCuMnS@CF) nanoarrays are fabricated by the mild cation exchange strategy. Benefiting from the synergistic effect among multiple metals and the strong interfacial bonding between high-entropy Co-Zn-Cd-Cu-Mn sulfide nanoarrays and the carbon fiber support, CoZnCdCuMnS@CF exhibits superior catalytic activity and stability toward overall water splitting in alkaline medium. Impressively, CoZnCdCuMnS@CF only needs low overpotentials of 173 and 220 mV to reach the current density of 10 mA•cm^{-2}, with excellent durability for over 70 and 113 h for hydrogen evolution reaction (HER) and oxygen evolution reaction (OER) respectively. More importantly, the bifunctional electrode (CoZnCdCuMnS@CF||CoZnCdCuMnS@CF) for overall water splitting can deliver a small cell voltage of 1.63 V to afford 10 mA•cm^{-2} and exhibit outstanding stability of negligible decay after 73 h continuous operation. This work provides a viable synthesis route toward advanced high-entropy materials with great potential applications.

KEYWORDS

electrocatalysis, high-entropy metal sulfides, oxygen evolution reaction, hydrogen evolution reaction, low-temperature cation exchange

1 Introduction

As an ideal energy alternative to traditional fossil fuels, hydrogen has attracted significant attention due to the high gravimetric energy density and zero carbon emission. Electrocatalytic water splitting is recognized as a promising strategy to convert natural water to hydrogen [1–3]. In general, the cathode hydrogen evolution reaction (HER) and the anodic oxygen evolution reaction (OER) constitute the two half-reactions of overall water splitting [4, 5]. To improve the efficiency of water electrolysis, developing non-precious and effective catalysts to accelerate the sluggish kinetics caused by HER and OER is highly desirable [6–8]. To date, transition metal sulfides (TMSs) have attracted great focus as the promising candidate for catalyzing overall water splitting due to the good electrical conductivity and favorable activity [9–11]. Various TMSs have been reported, such as unary, binary, ternary, and quaternary sulfides with heterogeneous structures [12–15]. Notably, ternary TMSs possess more advanced activity than unary and binary TMSs due to the synergistic effect [16]. Unfortunately, TMSs behave in poor electrochemical stability of structure and morphology, resulting in the detachment from substrate under high potential [17, 18]. In addition, the most reported TMSs composed of only a few metal elements lack extensive compositional adjustability. Therefore, the development of polymetallic yet stable TMSs for overall water splitting is particularly necessary.

Recently, high-entropy TMSs featuring homogeneously mixed multi-metallic elements, high entropy effect, good electrical conductivity, and single-phase structure have attracted much attention [19, 20]. Benefiting from the synergistic effect among multiple metals and the high-entropy effect, high-entropy TMSs are expected to improve catalytic activity, structure stability, and compositional tunability toward the optimal adsorption of reaction intermediates, compared with unary, binary, ternary, and quaternary TMSs [21]. In this regard, it is promising to optimize the catalytic performance for high-entropy TMSs through multiple-elemental synergy. However, the previous methods for the synthesis of high-entropy TMSs require high temperature to ensure the uniform mixing of various elements with different atomic radii, valence states, and oxidation potentials [22]. In addition, carbon supports as the current collector are indispensable in electrochemical energy conversion [23]. Therefore, rational design and synthesis of carbon-supported high-entropy TMSs at mild conditions can provide a new platform for overall water splitting.

Herein, we reported a low-temperature ion-exchange strategy

Address correspondence to shanghs@zzu.edu.cn

for the synthesis of carbon fiber supported high-entropy Co-Zn-Cd-Cu-Mn sulfide (CoZnCdCuMnS@CF) nanoarrays for the first time. The ion exchange is emerging as a high-efficient synthetic pathway for synthesizing a targeted structure, which is driven by the rapid ion diffusion in nanocrystal solids and exchange of one or more constituent elements to modify the composition while preserving the key structural characteristics of the template [24–26]. In our case, the Co-precursor@CF was synthesized by a typical hydrothermal reaction first and subsequently sulfided by Na_2S forming Co_9S_8@CF. Finally, the high-entropy CoZnCdCuMnS@CF nanoarrays were obtained by the cation exchange reaction of Co_9S_8@CF with Zn^{2+}, Cd^{2+}, Cu^{2+}, and Mn^{2+} at low temperature. As expected, the high-entropy CoZnCdCuMnS@CF nanoarrays achieve superior catalytic performance than the binary, ternary, and quaternary sulfides. In particular, the high-entropy CoZnCdCuMnS@CF nanoarray achieve the overpotential of 173 and 220 mV at 10 mA·cm^{-2} toward HER and OER, respectively. More importantly, the outstanding stability of high-entropy CoZnCdCuMnS@CF nanoarrays is also reflected by the 70 and 113 h tests for HER and OER. When using high-entropy CoZnCdCuMnS@CF as both the cathode and anode, it provides a current density of 10 mA·cm^{-2} at 1.63 V with durability for over 73 h. Our low-temperature cation-exchange strategy may shed light on the construction of other advanced high-entropy catalysts for electrocatalytic water splitting and beyond.

2 Experimental

2.1 Synthesis of Co-precursor@CF

The Co-precursor nanowire arrays were fabricated via a simple hydrothermal strategy. First, the carbon cloth (CC) was washed with acetone, ethanol, and ultra-pure water under sonication for 20 min, respectively. Then, $Co(NO_3)_2{\cdot}6H_2O$ (5 mmol), urea (25 mmol), and NH_4F (10 mmol) were added into 60 mL ultra-pure water under stirring. Then the homogeneous solution was transferred to a 100 mL Teflon-lined stainless steel autoclave accompanied by a prepared CC (2 cm × 3 cm), and the reaction system was carried out for 6 h at 120 °C. After cooling, the Co-precursor nanowire arrays grown on CF were washed with water and dried for 12 h at 60 °C.

2.2 Synthesis of Co_9S_8@CF

The Co_9S_8 nanowire arrays were prepared with a typical hydrothermal method. In this process, the Co-precursor@CF was immersed in 0.1 M $Na_2S{\cdot}9H_2O$ solution and taken into a 100 mL Teflon-lined stainless-steel autoclave to be heated at 120 °C for 8 h. After reacting and cooling, the obtained Co_9S_8 nanowire arrays were rinsed with ultra-pure water and dried at 60 °C.

2.3 Synthesis of CoZnCdCuMnS@CF

The CoZnCdCuMnS@CF sample was synthesized by the hydrothermal method of cation exchange. Specifically, 0.5 mmol $Zn(NO_3)_2{\cdot}6H_2O$, 0.03 mmol $CdCl_2{\cdot}2.5H_2O$, 0.03 mmol $Cu(NO_3)_2{\cdot}3H_2O$, 1 mmol $MnSO_4{\cdot}H_2O$ were all added into 60 mL ultra-pure water under stirring, and then the as prepared Co_9S_8@CF nanowires arrays was put into the clear and homogeneous solution. The mixture was transferred to a 100 mL Teflon-lined stainless-steel autoclave to be heated at 120 °C for 8 h. After reacting and cooling, the obtained CoZnCdCuMnS@CF nanowire arrays were washed with ultra-pure water and dried at 60 °C. The sample loading amount was measured by a microbalance to be 6.7 mg·cm^{-2}. For comparison, the mixing solution was replaced by the individual metal salt solution of $Zn(NO_3)_2{\cdot}6H_2O$, $CdCl_2{\cdot}2.5H_2O$, and $Cu(NO_3)_2{\cdot}3H_2O$, $MnSO_4{\cdot}H_2O$, respectively. And finally, the CoZnS@CF, CoZnCdS@CF, CoZnCdCuS@CF, CoCdS@CF, CoCuS@CF, and CoMnS@CF were synthesized at the same condition.

2.4 Characterization

X-ray diffraction (XRD) patterns were performed on Bruker D8 Advance (scan range of 5°–90°). Scanning electron microscopy (SEM) images were tested from an Ultra 55Zeiss field emission scanning electron microscope. The transmission electron microscopy (TEM) images were observed using a FEI Talos F200S emission scanning electron microscope. Raman spectra were acquired by LabRAM HR Evo with a 633 nm He-Ne laser. X-ray photoelectron spectroscopy (XPS) tests were obtained from an Escalab 250Xi electron spectrometer with Al Kα radiation.

2.5 Electrochemical measurements

The HER/OER experiments were performed by a three-electrode system on CHI 660E electrochemical workstation (1.0 M KOH), consisting of the Hg/HgO as the reference electrode, catalysts as the working electrode, and a graphite rod as the counter electrode, respectively. Linear sweep voltammetry (LSV) measurements were tested at 2 mV·s^{-1} toward HER and OER, respectively. 6.7 mg of commercial Pt/C and RuO_2 were added to the solution of 5% Nafion solution (50 μL) and ethanol (950 μL), respectively. The uniform ink was obtained by sonicating for 30 min and then loaded onto the bare CC (1 cm × 1 cm) to form the Pt/C and RuO_2 electrodes. The final potential was calibrated into reversible hydrogen electrode (RHE): E (vs. RHE) = E (vs. Hg/HgO) + 0.059pH + 0.098 (1.0 M KOH, pH = 14), and all LSV results were corrected with 85% iR compensation. The Nyquist plots of electrochemical impedance spectroscopy (EIS) were surveyed with alternating current (AC) impedance at 0.01–10^5 Hz for the frequency range. The electrochemical surface area (ECSA) were evaluated by cyclic voltammetry (CV) curves at the non-Faraday region from −0.7 to −0.9 V vs. Hg/HgO with different scan rates at 0.01, 0.02, 0.04, 0.06, 0.08, 0.1, and 0.12 V·s^{-1}. The stability measurements (v–t) were recorded at the constant current density of 10 mA·cm^{-2}.

3 Result and discussion

3.1 Synthesis and characterizations

The fabrication procedure of high-entropy CoZnCdCuMnS@CF nanoarrays using the facile cation exchange strategy is schematically illustrated in Fig. 1. In a typical experiment, the Co-precursor nanowires vertically grew on the carbon fibers via hydrothermal reaction firstly. Then Co-precursor nanowire array was converted to Co_9S_8 array with a sulfidation reaction at 120 °C [27]. Subsequently, the high-entropy CoZnCdCuMnS@CF nanoarray was fabricated by the cation exchange reaction between the Co_9S_8@CF and Zn^{2+}, Cd^{2+}, Mn^{2+}, Cu^{2+} ions. The possible reactions are proposed as follows in Eqs. (1)–(4)

$$Co_9S_8 + Cu^{2+} = CuS + Co^{2+} \quad (1)$$

$$Co_9S_8 + Cd^{2+} = CdS + Co^{2+} \quad (2)$$

$$Co_9S_8 + Zn^{2+} = ZnS + Co^{2+} \quad (3)$$

$$Co_9S_8 + Mn^{2+} = MnS + Co^{2+} \quad (4)$$

Notably, the reaction of Co_9S_8 (K_{sp} = 2.0 × 10^{-25}) with Cu^{2+} is more thermodynamically favorable than those with Cd^{2+}, Zn^{2+}, and Mn^{2+} ions, because the value of solubility follows the sequence of

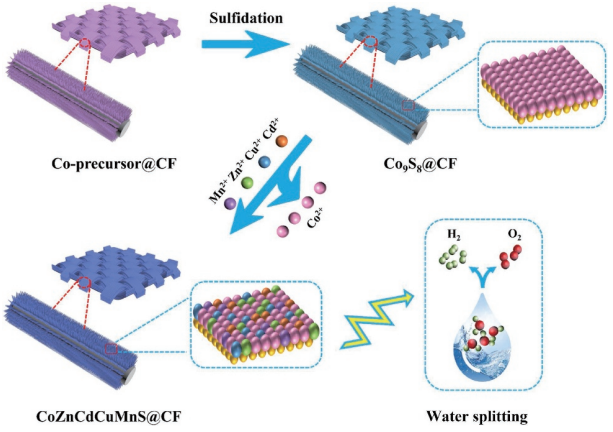

Figure 1 Schematic diagram of the synthesis process of CoZnCdCuMnS@CF.

CuS (K_{sp} = 6.3 × 10^{-36}) < CdS (K_{sp} = 8.0 × 10^{-27}) < ZnS (K_{sp} = 1.6 × 10^{-24}) < MnS (K_{sp} = 2.5 × 10^{-13}) [28, 29]. Herein, upon using a cation-exchange reaction, a completely homogeneous and single-phase high-entropy CoZnCdCuMnS@CF nanoarrays were obtained.

To clearly observe the morphology of the samples during the synthetic processes, SEM was conducted. The Co-precursors and Co_9S_8 vertical needle-like nanowire arrays were completely covered on the CF, as shown in Fig. S1 in the Electronic Supplementary Material (ESM), and the Co_9S_8@CF manifested a hollow structure. In this step, the outward diffusion effect during the sulfidation reaction was responsible for resulting in the hollow structure [12, 30, 31]. After cation exchange, the CoZnCdCuMnS@CF still retained the morphology of vertical needle-like nanowires, as shown in Figs. 2(a)–2(c). Furthermore, the quaternary CoZnCdCuS@CF was also obtained at the same reaction condition with CoZnCdCuMnS@CF except for the absence of Mn^{2+}, as displayed in Fig. S2 in the ESM. The TEM and elemental mappings were conducted to investigate the crystalline structure and elements distribution in CoZnCdCuMnS@CF. As shown in Figs. 2(d) and 2(e), the CoZnCdCuMnS@CF nanowires displayed a needle-like structure and rough surface. Furthermore, the interplanar distances of 0.574 and 0.352 nm were attributed to the (111) and (220) plane of CoZnCdCuMnS@CF in the crystalline area, as shown in Figs. 2(f) and 2(g), which was similar to that of pure Co_9S_8 [12, 32]. Interestingly, there was no lattice of other metal sulfides, indicating that the Zn, Cd, Mn, Cu were just incorporated in the lattice of Co_9S_8 and exchanged the Co out of Co_9S_8, forming a homogeneous single-phase in CoZnCdCuMnS@CF. Furthermore, the elemental mapping of CoZnCdCuMnS@CF suggested that Co, Zn, Cd, Mn, Cu, and S were uniformly distributed over the entire architecture (Fig. 2(h)). Notably, the lower content of Co in CoZnCdCuMnS@CF than that in Co_9S_8@CF (Figs. S3 and S4 in the ESM) reflected Co leached out of the Co_9S_8 lattice during the cation exchange reaction.

To identify the crystalline phases, XRD analysis was performed. As shown in Fig. 3(a), the major diffraction peaks corresponding to (311) and (440) planes in CoZnCdCuMnS@CF resemble those of Co_9S_8 (PDF#19-0364), indicating the formation of single-phase in CoZnCdCuMnS@CF [32]. Raman spectroscopy was employed to further exclude the impurity phases and the results are indicated in Fig. 3(b). Both the Raman spectra of CoZnCdCuMnS@CF and Co_9S_8@CF showed similar peaks at 194, 338, 465, 509, and 669 cm^{-1}, indicating the similar single phase of CoZnCdCuMnS@CF with Co_9S_8 [33, 34]. It is noted that the results of TEM, XRD, and Raman analysis proved the formation of single-phase high-entropy sulfide in CoZnCdCuMnS@CF.

The electronic interactions and valence states of the catalysts were evaluated by XPS analysis. Figure 3(c) and Fig. S5(a) in the ESM exhibited the survey spectra of CoZnCdCuMnS@CF and the references. It is evidenced that Co, Zn, Cd, Cu, Mn, and S elements existed in CoZnCdCuMnS@CF. In the spectra of S 2p (Fig. 3(d)), the fitting peaks at 161.85 and 163.0 eV were indexed to metal–sulfur bonds, while the peak at 169.75 eV could be attributed to the satellite peak [35–37]. The deconvoluted spectra of Co 2p (Fig. 3(e)) (i.e., Co $2p_{3/2}$ peaks at 778.9 and 781.85 eV and Co $2p_{1/2}$ peaks at 794 eV and 798.35 eV) suggested that the presence of Co^{3+} and Co^{2+} in Co_9S_8@CF and CoZnCdCuMnS@CF [30]. In addition to this, the area and intensity of Co^{2+} in CoZnCdCuMnS@CF decreased obviously compared to those of Co_9S_8@CF, indicating that Co^{2+} was exchanged out by Zn^{2+}, Cd^{2+},

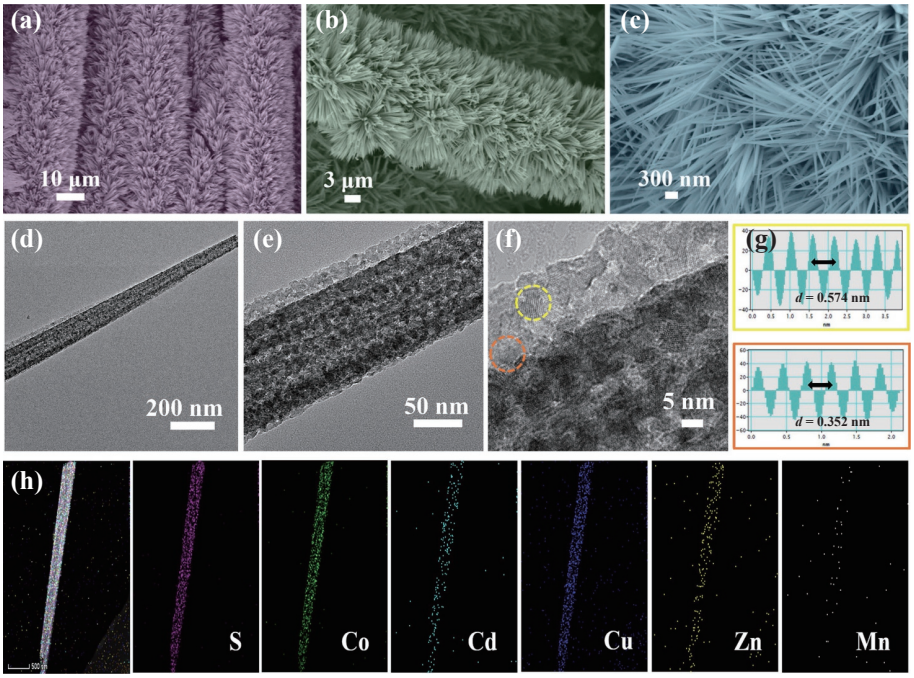

Figure 2 (a)–(c) SEM images of CoZnCdCuMnS@CF at various magnifications. (d)–(g) TEM images and the corresponding lattice spacing profiles at selected areas and (h) HAADF-STEM image with its corresponding elemental mapping images of CoZnCdCuMnS@CF.

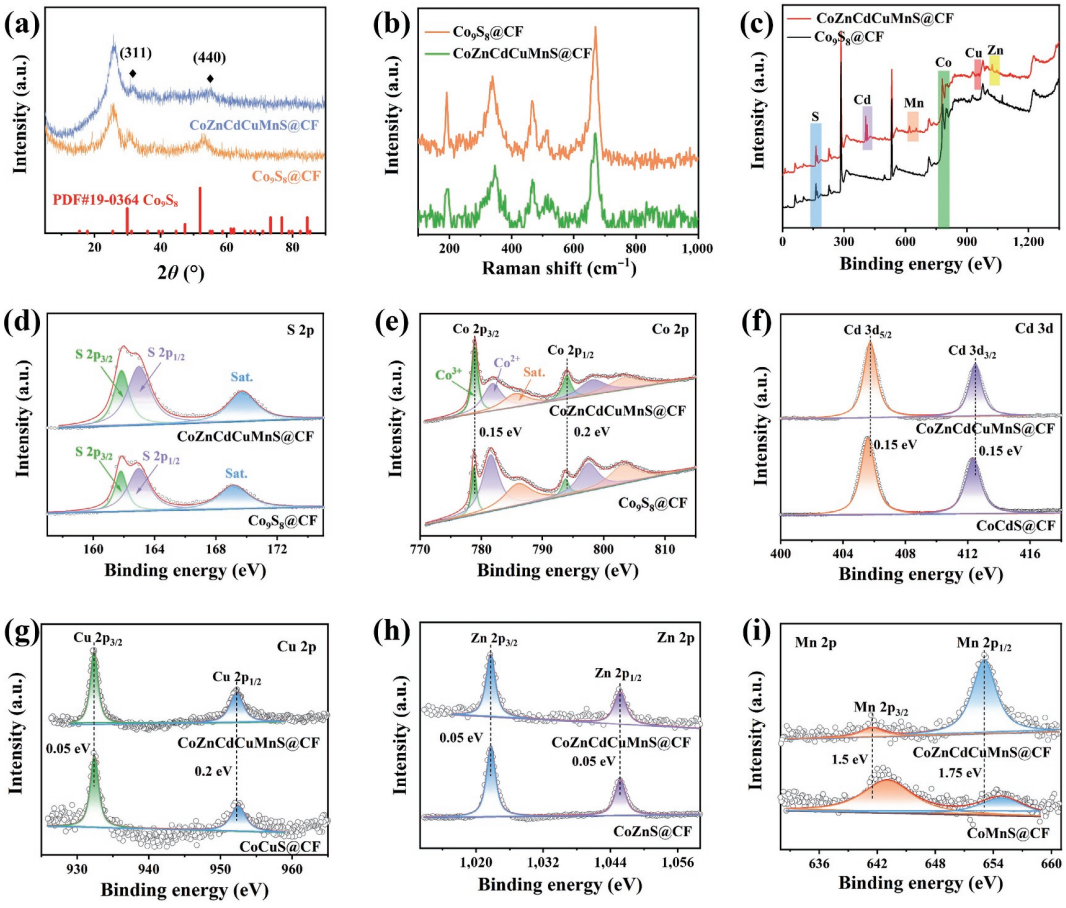

Figure 3 (a) XRD patterns and (b) Raman spectra of Co_9S_8@CF and CoZnCdCuMnS@CF. (c) XPS survey spectra, high-resolution XPS spectra for (d) S 2p, (e) Co 2p, (f) Cd 3d, (g) Cu 2p, (h) Zn 2p, and (i) Mn 2p of CoZnCdCuMnS@CF and the references.

Mn^{2+}, and Cu^{2+} during the cation exchange process. Furthermore, the Cd 3d, Cu 2p, Zn 2p and Mn 2p spectra also revealed the presence of Cd^{2+} (405.75 and 412.5 eV), Cu^{2+} (932.25 and 952.35 eV), Zn^{2+} (1022.6 and 1045.7 eV), and Mn^{2+} (641.5 and 653.05 eV) in CoZnCdCuMnS@CF and the corresponding references (Figs. 3(f)–3(i)) [38–41]. The above results illustrated that CoZnCdCuMnS@CF successfully formed after the cation-exchange reaction. Moreover, compared with other control samples (Figs. 3(f)–3(i) and Fig. S5(b) in the ESM), the shifts of the binding energy in CoZnCdCuMnS@CF further verified the existence of strong interactions between the multiple elements in CoZnCdCuMnS@CF [42–44]. Besides, the XPS spectra of CoZnCdS@CF and CoZnCdCuS@CF were shown in Figs. S6 and S7 in the ESM, the results indicated that the valence states of relating elements were similar to those of CoZnCdCuMnS@CF.

3.2 Oxygen evolution reaction measurement

To evaluate the catalytic performance of CoZnCdCuMnS@CF in OER, the two-electrode system was performed in 1.0 M KOH. As shown in Fig. 4(a), the CoZnCdCuMnS@CF exhibited a similar overpotential to that of RuO_2 at 10 mA·cm^{-2}, indicating the excellent OER performance of CoZnCdCuMnS@CF. Furthermore, the CoZnCdCuMnS@CF showed a lower overpotential of 220 mV at 10 mA·cm^{-2} compared to those of CoZnS@CF (276 mV), CoZnCdS@CF (267 mV), and CoZnCdCuS@CF (263 mV). Together with the results in Fig. S8(a) in the ESM, it is demonstrated that the electrocatalytic activity of the high-entropy CoZnCdCuMnS@CF is superior to those of corresponding unary, binary, ternary, and quaternary TMSs.

Tafel slope as an important kinetic parameter acquired from the LSV fitting was used to study the catalytic mechanism [45]. As depicted in Fig. 4(b) and Fig. S8(b) in the ESM, the high-entropy CoZnCdCuMnS@CF showed a smaller Tafel slope of 69.8 mV·dec^{-1} compared to those of binary CoZnS@CF (96.0 mV·dec^{-1}), ternary CoZnCdS@CF (89.0 mV·dec^{-1}), quaternary CoZnCdCuS@CF (72.2 mV·dec^{-1}), and the related samples. Thus, the Tafel analysis revealed the faster OER kinetics and higher catalytic activity of CoZnCdCuMnS@CF than those of controlled samples [46]. Compared with binary CoZnS@CF (276, 324, 349, and 367 mV), ternary CoZnCdS@CF (273, 319, 342, and 357 mV), quaternary CoZnCdCuS@CF (270, 330, 368, and 399 mV), the high-entropy CoZnCdCuMnS@CF only required lower overpotentials of 220, 271, 289 and 299 mV to achieve current densities of 10, 50, 100 and 150 mA·cm^{-2}, similar to the RuO_2 catalyst (211, 262, 297, and 327 mV) (Fig. 4(c)).

Figure 4(d) exhibited the comparison of the OER activity of CoZnCdCuMnS@CF with those of the reported (Table S1 in the ESM). The superior catalytic activity of CoZnCdCuMnS@CF is derived from the synergistic effect of the five metal elements, which modify the electronic structure toward the optimal adsorption of the intermediate products [19]. More importantly, CoZnCdCuMnS@CF also manifested excellent stability for 113 h test during OER (Figs. 4(e) and 4(f)), and the overpotential and Tafel slope after long-time operations declared an accepted change (Fig. S9 in the ESM), which is attributed to the reinforced interfacial bonding between high-entropy Co-Zn-Cd-Cu-Mn sulfide nanoarrays and the carbon fiber support. As another important parameter, ECSA was calculated by the double-layer capacitances (C_{dl}) via CV (Figs. S10 and S11 in the ESM) method to evaluate the performance of the electrocatalyst. As shown in Fig. 4(g) and Fig. S12 in the ESM, CoZnCdCuMnS@CF exhibited a C_{dl} value of 6.4 mF·cm^{-2}, which was much higher than those of

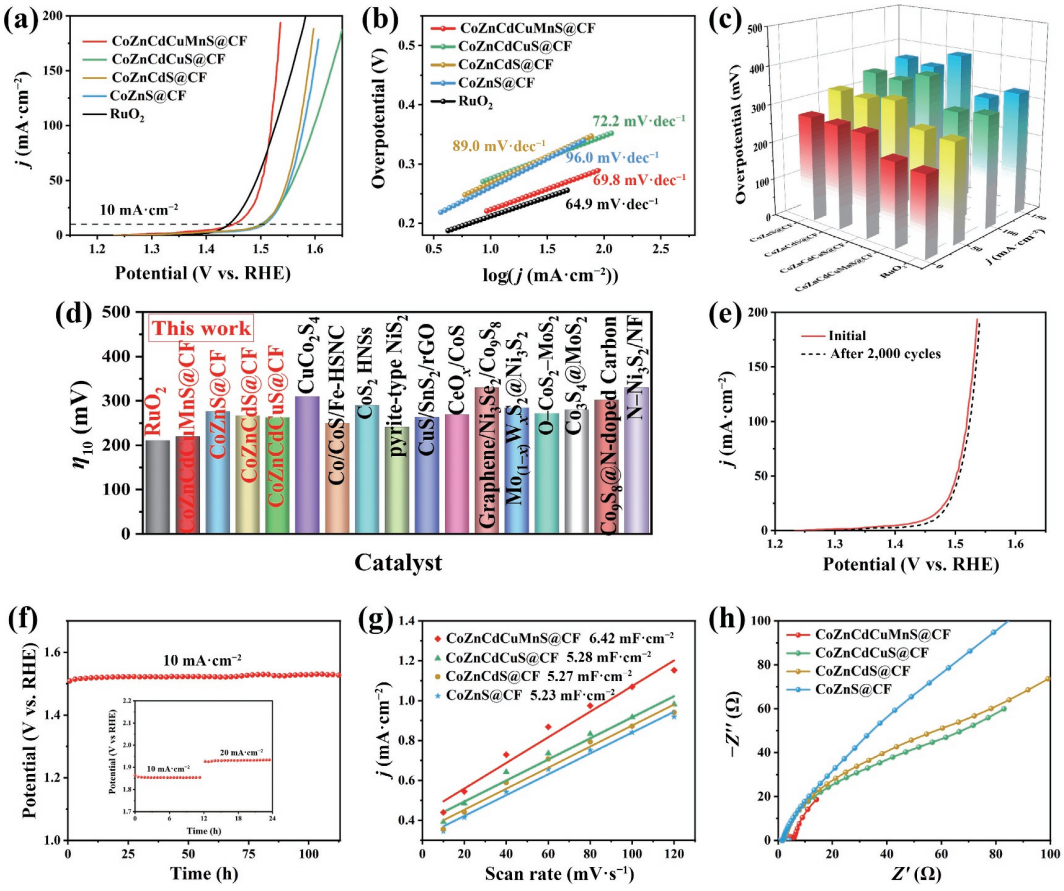

Figure 4 (a) OER polarization curves, (b) Tafel slopes, and (c) overpotentials of CoZnCdCuMnS@CF and the references at different current densities. (d) Comparison of overpotential (η_{10}) required to generate current density of 10 mA·cm^{-2} for CoZnCdCuMnS@CF, the references and reported catalysts. (e) Polarization curves of CoZnCdCuMnS@CF at the initial stage and after 2,000 cycling tests. (f) Long-term durability test of CoZnCdCuMnS@CF conducting at 10 mA·cm^{-2} (inset: chronopotentiometry curves conducted at various current densities). (g) C_{dl} values and (h) Nyquist plots of CoZnCdCuMnS@CF and the references.

binary CoZnS@CF (5.23 mF·cm^{-2}), ternary CoZnCdS@CF (5.27 mF cm^{-2}), quaternary CoZnCdCuS@CF (5.28 mF·cm^{-2}), and other samples, suggesting exposure of more active sites in high-entropy CoZnCdCuMnS@CF [47, 48]. In addition, EIS measurement presented that CoZnCdCuMnS@CF possessed a minimal Nyquist semicircle diameter than the control samples (Fig. 4(h) and Fig. S13 in the ESM), ensuring a rapid charge transfer between the electrolyte and the electrode [49, 50]

3.3 Hydrogen evolution reaction measurement

The HER performance of the as-synthesized samples was estimated in 1.0 M KOH. As displayed in Fig. 5(a) and Fig. S14(a) in the ESM, the high-entropy CoZnCdCuMnS@CF exhibited an overpotential of 173 mV at 10 mA·cm^{-2}, which was lower than those of binary CoZnS@CF (209 mV), ternary CoZnCdS@CF (204 mV), quaternary CoZnCdCuS@CF (198 mV), and the other samples. The Tafel slope of the as-synthesized samples was shown in Fig. 5(b) and Fig. S14(b) in the ESM. The high-entropy CoZnCdCuMnS@CF presented the smallest Tafel slope of 98.5 mV·dec^{-1}, compared to those of binary CoZnS@CF (108.6 mV·dec^{-1}), ternary CoZnCdS@CF (105.3 mV·dec^{-1}), quaternary CoZnCdCuS@CF (104.3 mV·dec^{-1}), and other samples. The lower Tafel slope indicated the faster reaction kinetics, which demonstrated the superior catalytic activity for high-entropy CoZnCdCuMnS@CF toward HER [51, 52]. To intuitively observe the differences of the overpotentials and Tafel slopes between high-entropy CoZnCdCuMnS@CF and the references, a comparison diagram was given in Fig. 5(c). Moreover, the HER stability of high-entropy CoZnCdCuMnS@CF catalysts was further investigated by chronopotentiometry, and the results showed that CoZnCdCuMnS@CF maintained excellent stability for 70 h at 10 mA·cm^{-2} with ignorable potential change (Fig. 5(d)). As shown in Fig. S15 in the ESM, the overpotential and Tafel slopes of high-entropy CoZnCdCuMnS@CF showed little change after long-time operation for 70 h, which further illustrated the extraordinary HER stability of the high-entropy CoZnCdCuMnS@CF.

3.4 Overall water splitting measurement

Additionally, due to the prominent activities for both OER and HER, the electrochemical overall water splitting performance of CoZnCdCuMnS@CF was also tested in 1.0 M KOH electrolytes. Figure 6(a) displayed the catalytic activity of overall water splitting in a two-electrode system with the CoZnCdCuMnS@CF electrocatalysts as both the cathode and anode (denoted as CoZnCdCuMnS@CF||CoZnCdCuMnS@CF). This electrolyzer afforded a current density of 10 mA·cm^{-2} at 1.63 V, which was comparable to that of Pt/C||RuO_2. As displayed in Fig. 6(b), the CoZnCdCuMnS@CF||CoZnCdCuMnS@CF electrolytic cell can achieve current densities of 10, 20, and 40 mA·cm^{-2} with corresponding voltages of 1.63, 1.72, and 1.78 V. Furthermore, a negligible change was observed for the CoZnCdCuMnS@CF electrolyzer in the 73 h chronopotentiometry test, illustrating the superior stability of the CoZnCdCuMnS@CF (Fig. 6(c)).

Additionally, the OER stability of the CoZnCdCuMnS@CF was further understood, and the detailed results were shown in Figs. 6(d) and 6(e). After the OER test, the morphology of CoZnCdCuMnS@CF was still well maintained (Fig. 6(d)), and the energy-dispersive X-ray spectroscopy (EDX) element mapping

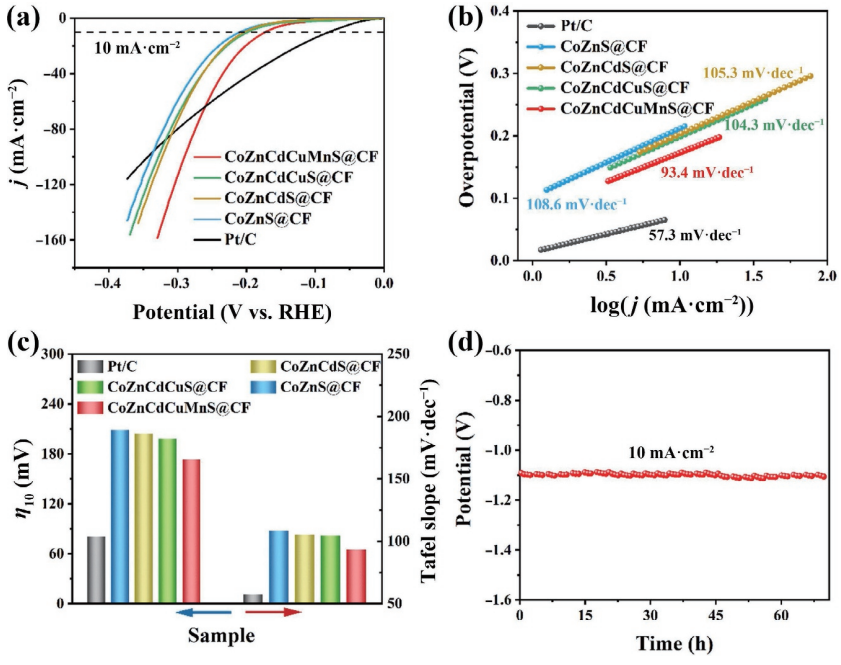

Figure 5 (a) Polarization curves toward the HER in 1.0 M KOH. (b) Tafel plots. (c) Summary of the overpotentials at 10 mA·cm^{-2} vs. RHE and Tafel slopes of relevant electrodes in this work. (d) HER chronoamperometry curve of CoZnCdCuMnS@CF in 1.0 M KOH.

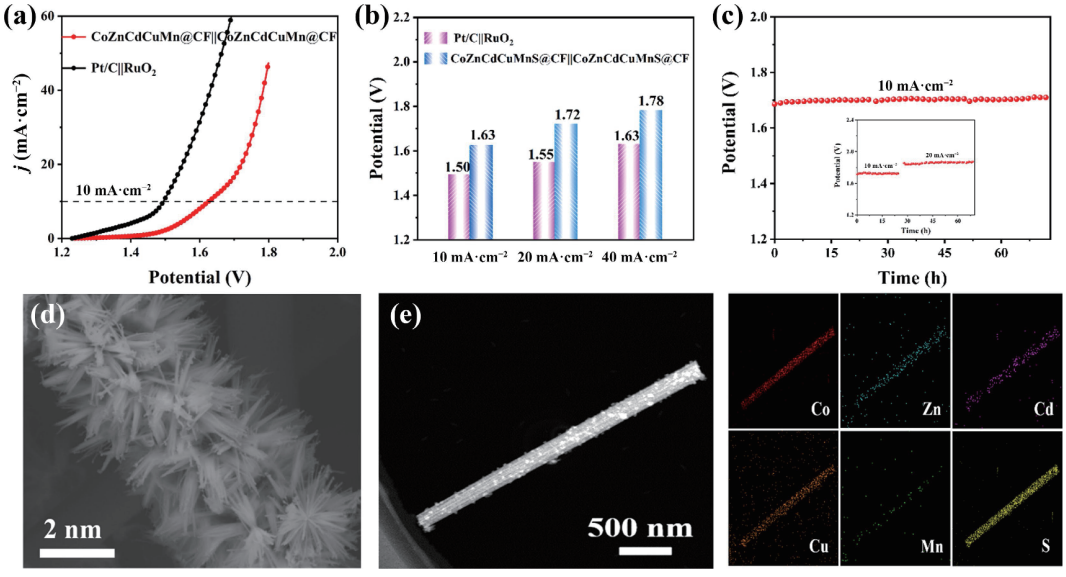

Figure 6 (a) Polarization curves of water splitting using CoZnCdCuMnS@CF as both anode and cathode in 1.0 M KOH. (b) The voltage requirements of the samples at current densities of 10, 20, and 40 mA cm^{-2}. (c) Chronopotentiometry (CP) curves with a constant current density of 10 mA·cm^{-2} for 73 h (inset: CP curves conducted at various current densities). (d) and (e) SEM, HAADF-STEM, and the corresponding EDX element mapping images for CoZnCdCuMnS@CF after the OER test.

images also identified the evenly distributed elements over the entire substrate (Fig. 6(e) and Fig. S16 in the ESM). Besides, the valence states of CoZnCdCuMnS@CF were well maintained after a 113 h stability test at 10 mA·cm^{-2} for OER, which were corroborated by XPS (Fig. S17 in the ESM). Moreover, the XRD and Raman (Figs. S18 and S19 in the ESM) confirmed that the structure of CoZnCdCuMnS@CF did not change after the HER and OER tests. All the above results proved that CoZnCdCuMnS@CF displayed excellent catalytic activity and durability during the overall water splitting process, which derived from the synergistic effect among multiple metals and the strong interfacial bonding between high-entropy Co-Zn-Cd-Cu-Mn sulfide nanoarrays and the carbon fiber support.

4 Conclusion

In summary, we synthesized homogeneously mixed high-entropy metal sulfides nanoarray supported on carbon fiber (CoZnCdCuMnS@CF) through a low-temperature cation exchange strategy. The facile cation exchange reactions enable partial Co^{2+} ions to leach out from the lattice of Co_9S_8. In the meantime, Zn^{2+}, Cd^{2+}, Cu^{2+} and Mn^{2+} ions were introduced and occupied the positions of leached Co atoms, forming homogeneously mixed and entropy-stabilized CoZnCdCuMnS@CF. The as-prepared CoZnCdCuMnS@CF performed excellent catalytic activity and durability toward HER and OER, benefitting by the synergy electronic regulation among the five metallic elements and the reinforced interfacial bonding between high-entropy Co-Zn-Cd-Cu-Mn sulfide nanoarrays and the carbon fiber support. Impressively, the catalyst exhibited overpotentials of 220 and 173 mV at 10 mA·cm^{-2} with excellent durability for over 113 and 70 h for OER and HER in alkaline medium. More importantly, CoZnCdCuMnS@CF required a

voltage of 1.63 V to afford 10 mA·cm^{-2} for overall water splitting. Overall, this work opens a new avenue for fabricating high-efficiency high-entropy materials for energy storage and conversion.

Acknowledgements

The authors thank the National Natural Science Foundation of China (No. U1804140), and China Postdoctoral Science Foundation (No. 2021M702939) for support.

Electronic Supplementary Material: Supplementary materials (additional SEM images, XRD patterns, TEM images, Raman spectrum, EDX spectra, XPS spectra, and electrochemical activities of relevant samples) is available in the online version of this article at https://doi.org/10.1007/s12274-022-4304-8.

References

[1] Seh, Z. W.; Kibsgaard, J.; Dickens, C. F.; Chorkendorff, I.; Nørskov, J. K.; Jaramillo, T. F. Combining theory and experiment in electrocatalysis: Insights into materials design. *Science* **2017**, *355*, 146.

[2] Yang, L.; Liu, R. M.; Jiao, L. F. Electronic redistribution: Construction and modulation of interface engineering on CoP for enhancing overall water splitting. *Adv. Funct. Mater.* **2020**, *30*, 1909618.

[3] Yan, H. J.; Xie, Y.; Wu, A. P.; Cai, Z. C.; Wang, L.; Tian, C. G.; Zhang, X. M.; Fu, H. G. Anion-modulated HER and OER activities of 3D Ni-V-based interstitial compound heterojunctions for high-efficiency and stable overall water splitting. *Adv. Mater.* **2019**, *31*, 1901174.

[4] Ma, S. F.; Huang, J.; Zhang, C.; Chen, G. L.; Chen, W.; Shao, T.; Li, T. T.; Zhang, X. H.; Gong, T.; Ostrikov, K. K. One-step *in-situ* sprouting high-performance $NiCoS_xSe_y$ bifunctional catalysts for water electrolysis at low cell voltages and high current densities. *Chem. Eng. J.* **2022**, *435*, 134859.

[5] Liu, H. T.; Guan, J. Y.; Yang, S. X.; Yu, Y. H.; Shao, R.; Zhang, Z. P.; Dou, M. L.; Wang, F.; Xu, Q. Metal-organic-framework-derived Co_2P nanoparticle/multi-doped porous carbon as a trifunctional electrocatalyst. *Adv. Mater.* **2020**, *32*, e2003649.

[6] Yang, Y.; Yao, H. Q.; Yu, Z. H.; Islam, S. M.; He, H. Y.; Yuan, M. W.; Yue, Y. H.; Xu, K.; Hao, W. C.; Sun, G. B. et al. Hierarchical nanoassembly of $MoS_2/Co_9S_8/Ni_3S_2$/Ni as a highly efficient electrocatalyst for overall water splitting in a wide pH range. *J. Am. Chem. Soc.* **2019**, *141*, 10417–10430.

[7] Zhang, B.; Shan, J. W.; Wang, W. L.; Tsiakaras, P.; Li, Y. Y. Oxygen vacancy and core–shell heterojunction engineering of anemone-like CoP@CoOOH bifunctional electrocatalyst for efficient overall water splitting. *Small*, in press, https://doi.org/10.1002/smll.202106012.

[8] Wang, Z. Y.; Yang, J.; Wang, W. Y.; Zhou, F. Y.; Zhou, H.; Xue, Z. G.; Xiong, C.; Yu, Z. Q.; Wu, Y. Hollow cobalt-nickel phosphide nanocages for efficient electrochemical overall water splitting. *Sci. China Mater.* **2020**, *64*, 861–869.

[9] Liu, G. L.; Robertson, A. W.; Li, M. M. J.; Kuo, W. C. H.; Darby, M. T.; Muhieddine, M. H.; Lin, Y. C.; Suenaga, K.; Stamatakis, M.; Warner, J. H. et al. MoS_2 monolayer catalyst doped with isolated Co atoms for the hydrodeoxygenation reaction. *Nat. Chem.* **2017**, *9*, 810–816.

[10] Cai, P. W.; Huang, J. H.; Chen, J. X.; Wen, Z. H. Oxygen-containing amorphous cobalt sulfide porous nanocubes as high-activity electrocatalysts for the oxygen evolution reaction in an alkaline/neutral medium. *Angew. Chem., Int. Ed.* **2017**, *56*, 4858–4861.

[11] Han, H.; Kim, K. M.; Choi, H.; Ali, G.; Chung, K. Y.; Hong, Y. R.; Choi, J.; Kwon, J.; Lee, S. W.; Lee, J. W. et al. Parallelized reaction pathway and stronger internal band bending by partial oxidation of metal sulfide-graphene composites: Important factors of synergistic oxygen evolution reaction enhancement. *ACS Catal.* **2018**, *8*, 4091–4102.

[12] Li, X. Y.; Li, K. K.; Zhu, S. C.; Fan, K.; Lyu, L. L.; Yao, H. M.; Li, Y. Y.; Hu, J. L.; Huang, H. T.; Mai, Y. W.; Goodenough, J. B. Fiber-in-tube design of Co_9S_8-carbon/Co_9S_8: Enabling efficient sodium storage. *Angew. Chem., Int. Ed.* **2019**, *58*, 6239–6243.

[13] Yang, D.; Cao, L. Y.; Feng, L. L.; Huang, J. F.; Kajiyoshi, K.; Feng, Y. Q.; Liu, Q. Q.; Li, W. B.; Feng, L.; Hai, G. J. Formation of hierarchical Ni_3S_2 nanohorn arrays driven by *in-situ* generation of VS_4 nanocrystals for boosting alkaline water splitting. *Appl. Catal. B-Environ.* **2019**, *257*, 117911.

[14] Liu, Y. K.; Jiang, S.; Li, S. J.; Zhou, L.; Li, Z. H.; Li, J. M.; Shao, M. F. Interface engineering of (Ni, Fe)S_2@MoS_2 heterostructures for synergetic electrochemical water splitting. *Appl. Catal. B-Environ.* **2019**, *247*, 107–114.

[15] Li, Y. Z.; Cao, R.; Li, L. B.; Tang, X. N.; Chu, T. L.; Huang, B. Y.; Yuan, K.; Chen, Y. W. Simultaneously integrating single atomic cobalt sites and Co_9S_8 Nanoparticles into hollow carbon nanotubes as trifunctional electrocatalysts for Zn-air batteries to drive water splitting. *Small* **2020**, *16*, e1906735.

[16] Cui, M. J.; Yang, C. P.; Li, B. Y.; Dong, Q.; Wu, M. L.; Hwang, S.; Xie, H.; Wang, X. Z.; Wang, G. F.; Hu, L. B. High‐entropy metal sulfide nanoparticles promise high‐performance oxygen evolution reaction. *Adv. Energy Mater.* **2021**, *11*, 2002887.

[17] Zhao, X.; Shang, X.; Quan, Y.; Dong, B.; Han, G. Q.; Li, X.; Liu, Y. R.; Chen, Q.; Chai, Y. M.; Liu, C. G. Electrodeposition-solvothermal access to ternary mixed metal Ni-Co-Fe sulfides for highly efficient electrocatalytic water oxidation in alkaline media. *Electrochim. Acta* **2017**, *230*, 151–159.

[18] Cui, Z. M.; Chen, H.; Zhao, M. T.; DiSalvo, F. J. High-performance Pd_3Pb intermetallic catalyst for electrochemical oxygen reduction. *Nano Lett.* **2016**, *16*, 2560–2566.

[19] Nguyen, T. X.; Su, Y. H.; Lin, C. C.; Ting, J. M. Self-reconstruction of sulfate-containing high entropy sulfide for exceptionally high-performance oxygen evolution reaction electrocatalyst. *Adv. Funct. Mater.* **2021**, *31*, 2106229.

[20] Liu, M. M.; Zhang, Z. H.; Okejiri, F.; Yang, S. Z.; Zhou, S. H.; Dai, S. Entropy-maximized synthesis of multimetallic nanoparticle catalysts via a ultrasonication-assisted wet chemistry method under ambient conditions. *Adv. Mater. Interfaces* **2019**, *6*, 1900015.

[21] Du, X. C.; Huang, J. W.; Zhang, J. J.; Yan, Y. C.; Wu, C. Y.; Hu, Y.; Yan, C. Y.; Lei, T. Y.; Chen, W.; Fan, C. et al. Modulating electronic structures of inorganic nanomaterials for efficient electrocatalytic water splitting. *Angew. Chem., Int. Ed.* **2019**, *58*, 4484–4502.

[22] Oses, C.; Toher, C.; Curtarolo, S. High-entropy ceramics. *Nat. Rev. Mater.* **2020**, *5*, 295–309.

[23] Li, T. Y.; Yao, Y. G.; Ko, B. H.; Huang, Z. N.; Dong, Q.; Gao, J. L.; Chen, W.; Li, J. G.; Li, S. K.; Wang, X. Z. et al. Carbon‐supported high‐entropy oxide nanoparticles as stable electrocatalysts for oxygen reduction reactions. *Adv. Funct. Mater.* **2021**, *31*, 2010561.

[24] Fenton, J. L.; Schaak, R. E. Structure-selective cation exchange in the synthesis of zincblende MnS and CoS nanocrystals. *Angew. Chem., Int. Ed.* **2017**, *56*, 6464–6467.

[25] Liu, Y.; Lim, C. K.; Fu, Z.; Yin, D. Q.; Swihart, M. T. Can the morphology of biconcave metal sulfide nanoplatelets be preserved during cation exchange. *Chem. Mater.* **2019**, *31*, 5706–5712.

[26] Li, X. Y.; Iqbal, M. A.; Xu, M.; Wang, Y. C.; Wang, H. Z.; Ji, M. W.; Wan, X. D.; Slater, T. J. A.; Liu, J.; Liu, J. J. et al. Au@$Hg_xCd_{1-x}Te$ core@shell nanorods by sequential aqueous cation exchange for near-infrared photodetectors. *Nano Energy* **2019**, *57*, 57–65.

[27] Yan, J. G.; Chen, L. G.; Liang, X. Co_9S_8 nanowires@NiCo LDH nanosheets arrays on nickel foams towards efficient overall water splitting. *Sci. Bull.* **2019**, *64*, 158–165.

[28] Jin, Y.; Chumanov, G. Synthesis of nonstoichiometric Cu_2ZnSnS_4 from ZnS by cation exchange. *Eur. J. Inorg. Chem.* **2017**, *2017*, 3761–3766.

[29] Li, X. Y.; Ji, M. W.; Li, H. B.; Wang, H. Z.; Xu, M.; Rong, H. P.;

Wei, J.; Liu, J.; Liu, J. J.; Chen, W. X. et al. Cation/anion exchange reactions toward the syntheses of upgraded nanostructures: Principles and applications. *Matter* **2020**, *2*, 554–586.

[30] Jia, H. N.; Wang, Z. Y.; Zheng, X. H.; Lin, J. H.; Liang, H. Y.; Cai, Y. F.; Qi, J. L.; Cao, J.; Feng, J. C.; Fei, W. D. Interlaced Ni-Co LDH nanosheets wrapped Co_9S_8 nanotube with hierarchical structure toward high performance supercapacitors. *Chem. Eng. J.* **2018**, *351*, 348–355.

[31] Wang, S. B.; Guan, B. Y.; Wang, X.; Lou, X. W. D. Formation of hierarchical Co_9S_8@$ZnIn_2S_4$ heterostructured cages as an efficient photocatalyst for hydrogen evolution. *J. Am. Chem. Soc.* **2018**, *140*, 15145–15148.

[32] Liu, Q.; Hong, X. D.; Zhang, X.; Wang, W.; Guo, W. X.; Liu, X. Y.; Ye, M. D. Hierarchically structured Co_9S_8@$NiCo_2O_4$ nanobrushes for high-performance flexible asymmetric supercapacitors. *Chem. Eng. J.* **2019**, *356*, 985–993.

[33] Li, W. Q.; Li, Y. H.; Fu, H. Q.; Yang, G. X.; Zhang, Q.; Chen, S. Z.; Peng, F. Phosphorus doped Co_9S_8@CS as an excellent air-electrode catalyst for zinc-air batteries. *Chem. Eng. J.* **2020**, *381*, 122683.

[34] Deng, S. J.; Zhong, Y.; Zeng, Y. X.; Wang, Y. D.; Wang, X. L.; Lu, X. H.; Xia, X. H.; Tu, J. P. Hollow TiO_2@Co_9S_8 core-branch arrays as bifunctional electrocatalysts for efficient oxygen/hydrogen production. *Adv. Sci.* **2018**, *5*, 1700772.

[35] Wang, S. Z.; Zhao, H. P.; Lv, S. Y.; Jiang, H. H.; Shao, Y. L.; Wu, Y. Z.; Hao, X. P.; Lei, Y. Insight into nickel-cobalt oxysulfide nanowires as advanced anode for sodium‐ion capacitors. *Adv. Energy Mater.* **2021**, *11*, 2100408.

[36] Kim, M.; Anjum, M. A. R.; Choi, M.; Jeong, H. Y.; Choi, S. H.; Park, N.; Lee, J. S. Covalent 0D-2D heterostructuring of Co_9S_8-MoS_2 for enhanced hydrogen evolution in all pH electrolytes. *Adv. Funct. Mater.* **2020**, *30*, 2002536.

[37] Shang, H. S.; Zhou, X. Y.; Dong, J. C.; Li, A.; Zhao, X.; Liu, Q. H.; Lin, Y.; Pei, J. J.; Li, Z.; Jiang, Z. L. et al. Engineering unsymmetrically coordinated Cu-S_1N_3 single atom sites with enhanced oxygen reduction activity. *Nat. Commun.* **2020**, *11*, 3049.

[38] Zhou, X. P.; Yin, L. X.; Dai, K. Q.; Gao, X. Y.; Feng, Y. N.; Zhao, Y. F.; Zhang, B. Preparation of Ni_2P on twinned $Zn_{0.5}Cd_{0.5}S$ nanocrystals for high-efficient photocatalytic hydrogen production. *J. Chem. Sci.* **2020**, *132*, 26.

[39] Rameshbabu, R.; Ravi, P.; Sathish, M. Cauliflower-like CuS/ZnS nanocomposites decorated g-C_3N_4 nanosheets as noble metal-free photocatalyst for superior photocatalytic water splitting. *Chem. Eng. J.* **2019**, *360*, 1277–1286.

[40] Fang, X. Y.; Cui, L. F.; Pu, T. T.; Song, J. L.; Zhang, X. D. Core–shell CdS@MnS nanorods as highly efficient photocatalysts for visible light driven hydrogen evolution. *Appl. Surf. Sci.* **2018**, *457*, 863–869.

[41] Vaizoğullar, A. İ. An effective photocatalytic and photoelectrochemical performance of β/γ-MnS/CdS composite photocatalyst for degradation of flumequine and oxytetracycline antibiotics under visible light irradiation. *J. Mater. Sci.* **2019**, *55*, 4005–4016.

[42] Zhan, C. H.; Xu, Y.; Bu, L. Z.; Zhu, H. Z.; Feng, Y. G.; Yang, T.; Zhang, Y.; Yang, Z. Q.; Huang, B. L.; Shao, Q. et al. Subnanometer high-entropy alloy nanowires enable remarkable hydrogen oxidation catalysis. *Nat. Commun.* **2021**, *12*, 6261.

[43] Zhang, L. L.; Lei, Y. T.; Zhou, D. N.; Xiong, C. L.; Jiang, Z. L.; Li, X. Y.; Shang, H. S.; Zhao, Y. F.; Chen, W. X.; Zhang, B. Interfacial engineering of 3D hollow $CoSe_2$@ultrathin $MoSe_2$ core@shell heterostructure for efficient pH-universal hydrogen evolution reaction. *Nano Res.*, in press, http://doi.org/10.1007/s12274-021-3887-9.

[44] Yu, J. Y.; Wang, A. Z.; Yu, W. Q.; Liu, X. Y.; Li, X.; Liu, H.; Hu, Y. Y.; Wu, Y. E.; Zhou, W. J. Tailoring the ruthenium reactive sites on N doped molybdenum carbide nanosheets via the anti-Ostwald ripening as efficient electrocatalyst for hydrogen evolution reaction in alkaline media. *Appl. Catal. B-Environ.* **2020**, *277*, 119236.

[45] Huang, S. C.; Meng, Y. Y.; Cao, Y. F.; Yao, F.; He, Z. J.; Wang, X. X.; Pan, H.; Wu, M. M. Amorphous $NiWO_4$ nanoparticles boosting the alkaline hydrogen evolution performance of Ni_3S_2 electrocatalysts. *Appl. Catal. B-Environ.* **2020**, *274*, 119120.

[46] Dai, K. Q.; Zhang, N.; Zhang, L. L.; Yin, L. X.; Zhao, Y. F.; Zhang, B. Self-supported Co/CoO anchored on N-doped carbon composite as bifunctional electrocatalyst for efficient overall water splitting. *Chem. Eng. J.* **2021**, *414*, 128804.

[47] Jia, Z.; Yang, T.; Sun, L. G.; Zhao, Y. L.; Li, W. P.; Luan, J. H.; Lyu, F.; Zhang, L. C.; Kruzic, J. J.; Kai, J. J. et al. A novel multinary intermetallic as an active electrocatalyst for hydrogen evolution. *Adv. Mater.* **2020**, *32*, e2000385.

[48] Cao, C. S.; Ma, D. D.; Xu, Q.; Wu, X. T.; Zhu, Q. L. Semisacrificial template growth of self‐supporting MOF nanocomposite electrode for efficient electrocatalytic water oxidation. *Adv. Funct. Mater.* **2018**, *29*, 1807418.

[49] Wang, D. L.; Li, H. P.; Du, N.; Hou, W. G. Single platinum atoms immobilized on monolayer tungsten trioxide nanosheets as an efficient electrocatalyst for hydrogen evolution reaction. *Adv. Funct. Mater.* **2021**, *31*, 2009770.

[50] Pang, Q. Q.; Niu, Z. L.; Yi, S. S.; Zhang, S.; Liu, Z. Y.; Yue, X. Z. Hydrogen-etched bifunctional sulfur-defect-rich ReS_2/CC electrocatalyst for highly efficient HER and OER. *Small* **2020**, *16*, e2003007.

[51] Wan, J. W.; Zhao, Z. H.; Shang, H. S.; Peng, B.; Chen, W. X.; Pei, J. J.; Zheng, L. R.; Dong, J. C.; Cao, R.; Sarangi, R. et al. *In situ* phosphatizing of triphenylphosphine encapsulated within metal-organic frameworks to design atomic Co_1-P_1N_3 interfacial structure for promoting catalytic performance. *J. Am. Chem. Soc.* **2020**, *142*, 8431–8439.

[52] Mao, J. J.; He, C. T.; Pei, J. J.; Chen, W. X.; He, D. S.; He, Y. Q.; Zhuang, Z. B.; Chen, C.; Peng, Q.; Wang, D. S. et al. Accelerating water dissociation kinetics by isolating cobalt atoms into ruthenium lattice. *Nat. Commun.* **2018**, *9*, 4958.